

# Numerical simulation of the fluid dynamics of 2D rigid body motion with the vortex particle method

Jeff D. Eldredge \*

*Mechanical and Aerospace Engineering, University of California, Los Angeles, 420 Westwood Plaza, Box 951597,  
Los Angeles, CA 90095-1597, United States*

Received 22 August 2005; received in revised form 23 June 2006; accepted 23 June 2006  
Available online 14 August 2006

---

## Abstract

A viscous vortex particle method is presented for computing the fluid dynamics of two-dimensional rigid bodies in motion. The Navier–Stokes equations are solved using a fractional step procedure. Smooth particles carry vorticity and exchange strength to account for convection and viscous diffusion. The spurious slip resulting from this half-step is identified with a surface vortex sheet, and the slip is eliminated by diffusing the sheet to adjacent particles. Particles are remeshed every few time steps to a Cartesian grid with a ‘body-ignorant’ interpolation using simple symmetric stencils. Kelvin’s circulation theorem remains enforced by accounting for the circulation leaked into the body during this procedure, and redistributing it to the particles in the subsequent sheet diffusion. The stability and convergence with respect to numerical parameters are explored in detail, with particular focus on the residual slip velocity. The method is applied to two problems that demonstrate its utility for investigating biological locomotion: a flapping elliptical wing with hovering insect kinematics, with good agreement of forces with previous simulations and experiments; and a three-linkage ‘fish’ undergoing undulatory mechanics.

© 2006 Elsevier Inc. All rights reserved.

*MSC:* 65M99; 76M23; 76D25; 76Z10

*Keywords:* Numerical methods; Vortex methods; Viscous incompressible flow; Flow–structure interaction; Biological locomotion; Immersed boundary methods

---

## 1. Introduction

The interaction of a fluid with a complex moving boundary arises frequently in mechanics, particularly in natural and biological systems: insect flight, aquatic locomotion, cardiopulmonary flows, flows through the human vocal tract, and countless others. Investigations are enhanced greatly by a complementary computational effort, particularly because of the difficulty of obtaining *in vivo* flow measurements in these systems.

---

\* Tel.: +1 310 206 5094; fax: +1 310 206 4830.

*E-mail address:* [eldredge@seas.ucla.edu](mailto:eldredge@seas.ucla.edu).

However, conventional computational approaches that rely on body-conforming grids are challenged by such evolving geometries. It is useful, then, to seek an alternative numerical methodology that is more naturally suited to such problems.

In this work, we are primarily motivated by investigations of the biological mechanics of mobility, such as used by insects, aquatic animals and bioinspired technological systems, in a moderate Reynolds number flow regime. Viscous and inertial processes are both important in these forms of locomotion, and vortex shedding plays a fundamental role. A complete solution of the fluid dynamics of such problems requires a three-dimensional unsteady simulation, fully coupled with a solution of the elastically deforming body. Therefore, the numerical approach taken must be capable of such challenging requirements. This paper, which demonstrates the use of the viscous vortex particle method, represents a first step towards this goal: the analysis of two-dimensional rigid bodies in motion. By focusing on the creation and subsequent transport and diffusion of vorticity, this method provides a unique perspective and a useful alternative to other velocity-based numerical methodologies. The velocity field is recovered from vorticity-bearing particles by the Biot–Savart integral, so boundary conditions at infinity are automatically enforced. The method possesses an inherent economy in the number of computational elements since vorticity is generally confined to regions near the bodies and in their wake. Though the focus of this present work is on two-dimensional rigid bodies, the method will be extended to deformable and three-dimensional problems in later work.

Compared to the rich history of experimental investigation of insect flight and aquatic locomotion, computational studies have only recently reached maturity. As is common with complex physical systems, research in this field has focused on progressively more difficult ‘building-block’ problems to advance the state of knowledge. For example, much has been learned from the basic flow produced by the pitching and plunging of a two-dimensional rigid foil, which may be representative of a section of a high aspect ratio wing. In this system, the time-varying translational velocity and angle of attack can be imposed via the free-stream velocity, allowing a stationary, body-fitted computational grid. This approach was taken by Gustafson and Leben [1], and more recently by Wang [2].

Several computational studies of greater complexity have also relied on a traditional body-fitted grid methodology. Sun and Tang [3] used a time-dependent, body-conforming grid to obtain a three-dimensional solution for the flow around a fruitfly wing, to compare with the mechanical wing measurements of Dickinson, Lehmann and Sane [4]. The Navier–Stokes equations, expressed in an inertial Cartesian coordinate system, were transformed to a body-fitted curvilinear system using a mapping that varied with time as the wing configuration changed. A similar approach was used by Liu and Kawachi [5] to investigate the aerodynamics around the wing of a hawkmoth, and compare with delayed stall experimental results [6]. A hawkmoth wing consists of fore and hind portions attached along a common axis, and an allowance for changes in the relative angle-of-attack between these portions presented an additional challenge for the grid algorithm. Numerical studies of the fruitfly wing were also conducted by Ramamurti and Sandberg [7], using a finite element solution of the governing equations in arbitrary Lagrangian–Eulerian (ALE) formulation. The ALE approach allows the near-wing grid to move as the wing does, but remeshing is still required to eliminate badly distorted elements.

Though such body-fitted approaches allow a direct enforcement of the boundary conditions, the grid generation is challenging, particularly for the large motions and deformations characteristic of insect flight. Thus, methods in which the boundary is immersed in a regular Cartesian grid have been a particularly active area of research. In these methods, the effect of the boundary is either imposed directly—via interpolation of the surface velocities to nearby grid points—or indirectly, through some sort of singularity distribution (such as forcing terms or a vortex sheet). In the context of insect flight, both artifices have been used. The finite volume approach developed by Udaykumar and Mittal and coworkers [8,9] is an example of a direct Cartesian grid method, in which cells near the interface are cut to enforce a sharp boundary. The method has been used to solve for the fluid motion produced by a pair of two-dimensional flapping wings [10]. A notable example of an indirect approach is the immersed boundary method of Peskin and coworker [11,12], wherein an elastic boundary is represented by the singular distribution of forces it applies to the fluid. The singularity is smoothed in order to transfer its effect from the boundary to the grid. Beyond its extensive use in heart mechanics, the method has been applied to swimming organisms [13], and recently to insect hovering [14]. Hybrid methods that exploit the advantages of a sharp interface and the convenience of a fixed grid have been

developed by Mohd-Yusof and coworkers [15,16] and Gilmanov and Sotiropoulos [17]. The latter investigators report excellent agreement in the forces on a three-dimensional flapping wing with the experiments of Birch and Dickinson [18].

Russell and Wang [19] have recently developed a Cartesian grid method that utilizes a vorticity–streamfunction formulation. Though it is not possible to impose both the no-throughflow and no-slip conditions directly in this approach, a streamfunction field can be found that satisfies the first condition, and no-slip enforced by generating an appropriate amount of vorticity [20]. In [19], a Poisson equation is solved for the streamfunction that accounts for its jump on the boundary; an approach that is similar in spirit is used in the present work, using particles in lieu of a grid.

Particle-based computational methods provide a distinct perspective from such grid-based schemes. Vortex particle methods, in particular, have been used extensively for inviscid simulations of aerodynamics when supplemented with a Kutta condition at a well-defined separation point (see the review of [21]). Their range of utility has been extended in the past fifteen years to direct numerical simulation of viscous wall-bounded flows by appealing to the physical mechanism of vorticity generation at a no-slip surface (see Koumoutsakos [22] and references therein). Among the methods developed, the primary differences in implementation are in the treatment of viscous processes—both in how vorticity is created at the body surface and how it is fluxed into the fluid. Koumoutsakos, Leonard and Pépin [23] developed an approach that embodies the Lighthill creation mechanism: spurious slip on the body surface is manifested in a vortex sheet, and this sheet subsequently diffuses into the flow to enforce the no-slip condition. Viscous diffusion within the fluid is treated with the method of particle strength exchange [24]. Some refinement to this methodology has been made in later work by Ploumhans and Winckelmans [25] and Cottet, Koumoutsakos, and Salihi [26]. In both [23,25], emphasis was placed on particle configurations that conformed to the body surface with body-fitted interpolation stencils. In recent work, investigators have explicitly identified the immersed boundary principle that is inherent in the vorticity flux mechanism [27,22]. Indeed, the vorticity flux serves a role similar to the distributed forces that enforce no-slip in immersed boundary methods, and an alternative approach has been developed in which such a forcing term is added directly to the vorticity equation [27].

The present method will utilize the vorticity creation, convection and diffusion techniques of Koumoutsakos, Leonard and Pépin [23] and Ploumhans and Winckelmans [25]. The distinction of the present approach, however, is its retention of a simplified particle treatment near the boundary. This approach is similar to the vortex-in-cell method recently developed by Cottet and Poncet [27] in terms of its use of symmetric interpolation stencils. Both methods rely on the self-correcting aspect of the vorticity flux within the fractional-step methodology. In the present method, each body is arbitrarily situated relative to an initially Cartesian arrangement of particles. When the particle configuration must be remeshed, the interpolation of the old strengths to the new particles is carried out everywhere with the same symmetric stencils; the consequent leakage of particle strength into the body and the creation of spurious slip at the boundary are simply compensated for with additional vorticity flux immediately after the remeshing.

The numerical methodology and implementation, including the enforcement of boundary conditions and the particle remeshing procedure, are described in Section 2. Some further discretization details are included in Appendix A. The choice of numerical parameters is discussed in detail in Section 3, and the convergence of the residual slip on the boundary, after the vortex sheet diffusion, is analyzed in this section. The results from applying the method to two model problems—a single flapping wing with hovering insect kinematics, with comparison with numerical and experimental results from Wang, Birch and Dickinson [28], and the prescribed undulatory motion of a three-linkage fish (inspired by the recent inviscid analysis of aquatic locomotion by Kanso et al. [29])—are presented in Section 4, and discussed in detail.

## 2. Numerical methodology

The present implementation of the viscous vortex particle method (VVPM) is described in moderate detail in this section. Further mathematical details of many aspects of the basic methodology can be found in [30]. Consider a set of two-dimensional rigid bodies,  $j = 1, \dots, N_b$ , with respective translational velocity  $\mathbf{U}_j$  and angular velocity  $\boldsymbol{\Omega}_j$  (about centroid  $\mathbf{X}_j$ ). The region occupied by body  $j$  is denoted by  $\mathcal{A}_j$ , and the external

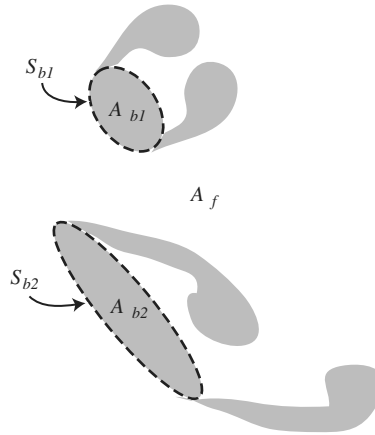


Fig. 1. The extended vorticity field.

region occupied by the fluid is denoted by  $\mathcal{A}_f$ . Thus, the whole space can be regarded as  $\mathbb{R}^2 = \mathcal{A}_f \cup \bigcup_{j=1}^{N_b} \mathcal{A}_j$ , with the boundary of each region denoted by  $\mathcal{S}_j$  (see Fig. 1).

In the vortex particle method, the Navier–Stokes equations are discretized by  $N_v$  regularized particles, or *blobs*, of vorticity. The particles are initially arranged on a Cartesian grid with uniform spacing  $\Delta x$ . Each blob is represented by a second-order-accurate Gaussian cutoff function, evaluated efficiently from a look-up table. The positions and strengths of the particles evolve according to the discretized convection and diffusion operations in the Navier–Stokes equations, respectively. The velocity field is composed, through the Biot–Savart integral, of contributions from vorticity in the fluid region, contained inside each body,  $2\Omega_j$ , and bound to the vortex sheet lying on each surface; in addition, an arbitrary potential flow can always be included (for example, a uniform flow,  $U_\infty$ ). A fast adaptive multipole method [31] is used to accelerate the Biot–Savart velocity field calculation to  $O(N_v)$ . Other components of the method, involving panel–panel and panel–particle interactions, are similarly accelerated. The technique of particle strength exchange (PSE) [24,32] with a second-order-accurate kernel is used to treat viscous diffusion within the flow.

### 2.1. Vorticity creation and the no-slip condition

In the impulsive start of a body, with zero initial vorticity in  $\mathcal{A}_f$ , the kinematic condition of no through-flow furnishes the strength,  $\gamma$ , of a vortex sheet that represents the spurious slip on the body surface. An integral equation for the vortex sheet strength is formed by matching the tangential component of the Biot–Savart velocity, evaluated on the body side of the sheet, with that of the local body velocity. For rigid bodies, the local velocity on body  $i$  is  $\mathbf{u}_b(\mathbf{x}) = \mathbf{U}_i + \boldsymbol{\Omega}_i \times (\mathbf{x} - \mathbf{X}_i)$ . The spurious slip velocity can be removed by fluxing the vortex sheet off the surface and into  $\mathcal{A}_f$ , so that continuity of the tangent component is thereby satisfied on the fluid side of the surface [33,34].

The vorticity flux process must be carried out in respect of Kelvin’s circulation theorem, which provides a constraint on the total sheet strength to be solved for each body,

$$\oint_{\mathcal{S}_j} \gamma(s) ds = -2A_j(\Omega_j(t + \Delta t) - \Omega_j(t)) + \Gamma_{\text{lost},j}. \tag{1}$$

The additional term,  $\Gamma_{\text{lost},j}$ , is used to correct for circulation leaked into the body during the particle remeshing, to be described in Section 2.2. The integral equation for the vortex sheet strengths is solved by discretizing the surface integrals using  $N_p$  linear panels with piecewise constant strengths. The resulting  $N_p$  equations, together with the  $N_b$  constraints, are solved in a least-squares sense. The details of this solution procedure are explained in Appendix A.

The vortex sheet is diffused into the fluid with the Neumann boundary condition  $-v\partial\omega/\partial n = \gamma/\Delta t$ , where the normal direction is into the fluid. The present method utilizes a semi-analytical scheme developed by Leon-

ard et al. [35], in which the vorticity fluxed over a time increment  $[0, \Delta t]$  from a flat panel is parceled to adjacent particles. A correction is added to each particle in the vicinity of the panel to ensure strict conservation of the distributed panel strength [25].

## 2.2. Body-ignorant particle remeshing

Particles are occasionally ‘remeshed’ to a new set of particles in a uniform Cartesian configuration, in order to preserve the overall accuracy of the numerical method and allow a tunable control of the particle population growth. In this work, this procedure is carried out at uniform time increments,  $\Delta t_r$ , using the fourth-order-accurate  $M'_4$  kernel originally developed for use in smoothed particle hydrodynamics [36]. The stencil of this kernel is four particles wide, with the original particle falling inside the second and third positions. The multi-dimensional kernel is constructed as a Cartesian product of the one-dimensional forms.

The presence of a body introduces some ambiguity to this interpolation procedure. Particles within one or two particle spacings from a body surface do not have a complete set of new particles within their stencil, and therefore the straightforward use of the symmetric kernel will effectively leak circulation into the body. Koumoutsakos and Shiels [37] and Ploumhans and Winckelmans [25] used specially-tailored kernels in the body vicinity to avoid such leakage; such special treatment was necessary in the flat plate simulations of [37].

In the present work we adopt a ‘body-ignorant’ strategy: the symmetric kernel is used everywhere to interpolate the strength of all particles onto the new set. The circulation leaked into each body during this process,  $\Gamma_{\text{lost},j}$ , is accounted for by adding the particle strengths interpolated to all stencil locations inside that body. This leaked circulation is used in the constraint (1) imposed on the vortex sheet solution immediately following this remeshing. Kelvin’s circulation theorem is thereby enforced when this sheet is subsequently diffused to the new particles. Though the locally leaked circulation is redistributed by this procedure to a larger region surrounding the body, the vorticity flux removes any spurious slip associated with this redistribution. This will be verified by convergence testing in Section 3.

The growth of the number of computational particles is controlled in two stages within the remeshing process:

- (1) New particles are only created from interpolation stencils of old particles, and only those outside of bodies are kept.
- (2) A ‘trimming’ procedure is used after remeshing to eliminate any new particle that satisfies *all* of the following criteria:
  - The particle’s strength (scaled by viscosity) is below a given threshold,  $|\Gamma_p|/\nu < \epsilon_{\text{trim}}$ .
  - The strengths of all particles *within a viscous radius*,  $R_v = 2C_v\sqrt{\nu\Delta t_r}$ , are below the same threshold.
  - The particle is not within  $R_v$  of any body.

This trimming procedure is carefully tailored to provide layers of zero strength particles at the periphery of the particle-covered region, as well as adjacent to each body. New particles that are within a distance  $C_g\Delta x$  of a body are treated as lying inside the body and eliminated to avoid problems with panel and particle singularities becoming too near each other. The factor  $C_g$  is set at 0.5, though the effect of this choice on residual slip will be explored in Section 3. The trimming threshold,  $\epsilon_{\text{trim}}$ , is generally chosen to be  $3 \times 10^{-3}$  or smaller; this choice will be evaluated in a specific problem in Section 4.1. The results are insensitive to the viscous radius provided  $C_v > 1$ ; a value of 2.5 is used throughout this work.

## 2.3. Calculation of forces

Vorticity-based numerical methods for incompressible flow focus on the vorticity transport equation rather than the velocity–pressure form of the Navier–Stokes equations, so pressure is generally not computed. Thus, the calculation of aerodynamic forces and moments must rely on alternative expressions. Surface integrals for the pressure are reformulated in terms of vorticity flux through use of the local momentum equation. The force on body  $j$  is

$$\mathbf{F}_j^f = \mu \oint_{\mathcal{A}_j} \left[ (\mathbf{x}_s(s) - \mathbf{X}_j) \times \frac{\partial \boldsymbol{\omega}}{\partial n}(s) - \mathbf{n}(s) \times \boldsymbol{\omega}(s) \right] ds + \rho \mathcal{A}_j \dot{\mathbf{U}}_j. \tag{2}$$

As before,  $\mathbf{n}$  is the local normal vector pointing into  $\mathcal{A}_j$ , and  $\mu$  is the dynamic viscosity of the fluid. The first term in the integral, together with the final inertial term, account for the effect of pressure; the second term represents the effect of the viscous shear stress. This formula has also been used in vortex particle methods by Koumoutsakos [38] and, in slightly different form, in the vorticity-based Cartesian grid method of Russell and Wang [19]. A similar derivation leads to a formula for the aerodynamic moment on  $j$  about the fixed origin,

$$\begin{aligned} M_j^f|_0 = & \mu \oint_{\mathcal{A}_j} \left[ \mathbf{x}_s(s) \times \left( \frac{1}{2} \mathbf{x}_s(s) \times \frac{\partial \boldsymbol{\omega}}{\partial n}(s) - \mathbf{n}(s) \times \boldsymbol{\omega}(s) \right) \right] \cdot \mathbf{e}_z ds - 4\mu \mathcal{A}_j \Omega_j + \rho \dot{\Omega}_j (|\mathbf{X}_j|^2 \mathcal{A}_j + 2B_j) \\ & + \rho \mathcal{A}_j (\mathbf{X}_j \times \dot{\mathbf{U}}_j) \cdot \mathbf{e}_z, \end{aligned} \tag{3}$$

where  $B_j$  is the second area moment of body  $j$ . These surface integrals are discretized using the same panels employed elsewhere in the numerical method. The vorticity at a panel centroid is computed by evaluating the streamfunction field—contributed by the *non-regularized* vortex particles, body vorticity, and uniform flow—at a set of points arranged uniformly along the normal direction from the centroid. The normal derivative of the vorticity is replaced with the vortex sheet strength using  $-\partial\omega/\partial n = \gamma/\Delta t$ . The vorticity flux contains an unphysical component to account for leaked circulation in remeshing steps; therefore, the force is only computed after non-remeshed steps.

### 3. Convergence and parameter choices

Numerical studies are conducted in this section to characterize the effect of the simplified body treatment of the method. These studies are used to examine the stability and rate of convergence with respect to numerical parameters, particularly the particle spacing,  $\Delta x$ , and time-step size,  $\Delta t$ . The influence of the particle-surface interaction is most clearly observable in the residual slip, the mismatch of tangential velocity between the body and the fluid *after* the incremental vortex sheet has been diffused. In order to explore this feature in a rather challenging example, the target of study of this section is an impulsive flow of velocity  $V$  past a 10:1 ellipse, normal to its major axis. The Reynolds number is 200, based on the length of the major axis,  $c$ . Two aspects of this problem serve as trouble spots for the VVPM (as well as other immersed boundary methods): the small radius of curvature of the edge of the body (which, in this ellipse, is  $a/100$ , where  $a$  is the semimajor axis,  $a = c/2$ ), and the non-uniform distance of particles from the body. The latter aspect proves most troublesome in regions where the boundary slope is slight compared with the Cartesian axes, where the particles have a ‘stair-step’ configuration.

The surface of the ellipse is discretized with  $N_p$  variably-sized panels, using a stretched circle parameterization  $(x_p, y_p) = (a \cos \phi_p, b \sin \phi_p)$ , where  $b$  is the semiminor axis, and  $\phi_p$  is uniformly distributed between 0 and  $2\pi$ . The panel sizes are given by the Jacobian,

$$\Delta s_p = \frac{2\pi}{N_p} (a^2 \sin^2 \phi_p + b^2 \cos^2 \phi_p)^{1/2}, \tag{4}$$

so the ratio of largest to smallest panel size is  $a/b$ . Error is quantified here with the  $L_2$  and  $L_\infty$  norms of the residual slip velocity on the body surface, normalized by the slip that exists at the instant of impulsive motion (prior to initial vorticity creation),

$$\varepsilon_{s,n} = \frac{\|\Delta u_{\text{slip}}\|_n}{\|\Delta u_{\text{slip}}^0\|_n}, \tag{5}$$

where  $n$  is either 2 or  $\infty$ . The discrete  $L_2$  norm is weighted by the panel sizes and divided by the perimeter. For the motion considered here, it can be shown that the initial slip is

$$\Delta u_{\text{slip}}^0(\phi) = \gamma^0(\phi) = V(a+b)(a^2 \sin^2 \phi + b^2 \cos^2 \phi)^{-1/2} \cos \phi, \tag{6}$$

so for  $a/b = 10$ ,  $\|\Delta u_{\text{slip}}^0\|_2 = 1.7954$  and  $\|\Delta u_{\text{slip}}^0\|_\infty = 11$ .



The parameters explored in this section are the particle spacing,  $\Delta x$ ; the time step size,  $\Delta t$ ; the remeshing interval,  $\Delta t_r$ ; the number of panels,  $N_p$ ; and the fractional gap between particles and body,  $C_g$ . The effect of the fractional gap,  $C_g$ , can be seen in Fig. 2, which depicts  $\varepsilon_{s,\infty}$  after 80 time steps, for  $\Delta x/c = 10^{-3}$  and  $V\Delta t/c = 10^{-4}$ . The residual slip remains relatively insensitive to this gap when it is below half of one particle spacing. However, the error drops significantly when  $C_g = 0.5$ , and then rises gradually beyond this gap size. For the remainder of the simulations, the fractional gap size is held at  $C_g = 0.5$ .

As with other numerical methods, stability requires an upper bound on the diffusion parameter,  $v\Delta t/\Delta x^2$ , determined by the particular time integration scheme used. It is important to note that the vorticity creation process of the VVPM implies a lower bound on this parameter, as well. The temporal boundary layer of thickness  $\sim \sqrt{4v\Delta t}$  created during each time step must extend beyond at least one particle spacing. When this layer is too thin, the transfer of vorticity from each panel to the neighboring particles is dominated by the correction to the sheet diffusion and the simulation becomes unstable. Thus, the time step size is restricted from above and below by these diffusion bounds,

$$D_{\min} < v\Delta t/\Delta x^2 < D_{\max}. \quad (7)$$

The value of  $D_{\min}$  depends on the geometry of the body and the panel discretization. In the case of the 10:1 ellipse, for example, the instability begins in the region depicted in Fig. 3, where particles are arranged in shallow stair-steps relative to the body. As evident in the case shown, the instability wavenumber is approximately the Nyquist frequency of the panels in that region. As the panel resolution increases, the value of  $D_{\min}$  decreases, but this decrease levels off at around 0.1 as the size of the largest panels approaches the particle spacing,  $\Delta x/\Delta s_{\max} \nearrow 1$ . This occurs when  $N_p\Delta x/c = \pi$  with the panel discretization of Eq. (4). In practice, setting  $D_{\min} = 0.2$  and  $D_{\max} = 1.2$ , with  $N_p\Delta x/c > 1.5$  (i.e. the size of the largest panel is less than twice the particle spacing) has led to stable results in all cases, using either fourth-order or second-order Runge–Kutta time integration.

It is important to note that the diffusion restrictions on  $\Delta t$  must be considered in tandem with the upper bound on the remeshing interval,  $\Delta t_r$ , which is dictated by its dual requirements: the maintenance of sufficient overlap of particles and the introduction of new layers of zero-strength particles to allow the diffusion front to progress. The latter requirement introduces another diffusion parameter restriction,

$$v\Delta t_r/\Delta x^2 < D_{r,\max}. \quad (8)$$

When  $\Delta t_r$  exceeds this bound, vorticity tends to become artificially confined at the particle periphery; since PSE is conservative, no circulation is lost. Provided that the particle Reynolds number,  $Re_p = |\omega|_{\max}\Delta x^2/v$ , is of order unity—as needed for a well-resolved simulation [25]—then convective and diffusive processes are

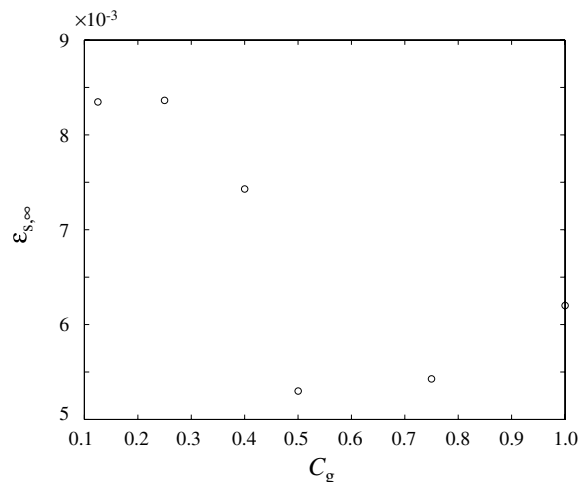


Fig. 2. Normalized  $L_\infty$  norm of residual slip versus the fractional gap between particles and body surface, after 80 time steps.

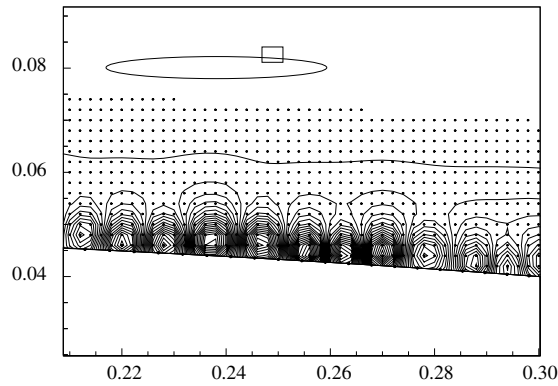


Fig. 3. Example of instability. Vorticity contours, panel centerpoints, and particles in the region depicted by the box, for  $v\Delta t/\Delta x^2 = 0.125$  and  $N_p\Delta x/c = 1.2$ .

locally in balance. Thus, the maintenance of overlap and the rate of introduction of new zero-strength particles can be simultaneously achieved with the same remeshing interval. Remeshing every 4–6 time steps has been found to be sufficient.

The time step size can only vary by at most one order of magnitude while spatial resolution is held fixed, due to the restriction in Eq. (7). Convergence of the residual slip is therefore evaluated with  $\Delta t$  and  $\Delta x$  both changing such that  $v\Delta t/\Delta x^2 = 1$ . This convergence is demonstrated in Fig. 4, which depicts  $\varepsilon_{s,2}$  evaluated at  $Vt/c = 0.0128$ , for both a 10:1 ellipse and a circular cylinder. For the elliptical body, the residual slip decays like  $\Delta x^{1.5}$ , but the decay rate is approximately  $\Delta x^{1.15}$  for the circular cross-section. The difference in these rates is attributable to the residual slip at the edges of the ellipse, whose strong contribution to the  $L_2$  norm decays more rapidly than on the rest of the body surface. First-order convergence is not surprising, in light of the diffusion of surface vorticity to scattered particles in the vicinity. It is likely that this can be improved using, e.g., tools developed for the immersed interface method [39]. Though it is not shown, it is important to mention that the residual difference in normal velocity has very similar magnitude and follows similar trends in all cases.

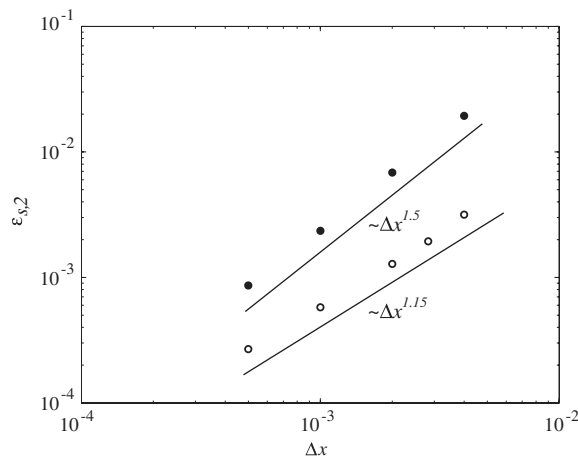


Fig. 4. Normalized  $L_2$  norm of residual slip versus particle spacing, evaluated at  $Vt/c = 0.0128$ , with  $v\Delta t/\Delta x^2 = 1$  for each case. Body aspect ratio 10: ●; 1: ○.



## 4. Results and discussion

In this section, the utility of the present method is demonstrated on two problems involving arbitrary motion of two-dimensional rigid bodies in a viscous fluid. The first, the flapping of a single elliptical wing, is motivated by the study of hovering insect flight aerodynamics, by identifying the rigid shape with the transverse section of an insect wing. The fluid forces obtained from VVPM simulations are compared with results from two-dimensional simulations and three-dimensional experiments recently carried out by Wang, Birch and Dickinson [28]. The second example is a viscous simulation of a three-linkage ‘fish’ moving in a trajectory that was recently established in an inviscid analysis by Kanso et al. [29]. It should also be noted that the methodology described in this paper has been validated on the benchmark problem of flow past an impulsively started cylinder; the results of this validation problem, using similar forms of this methodology, have been presented in previous work [23,25], and are omitted from this paper for brevity.

### 4.1. Flapping elliptical wing

In this set of simulations, a single elliptical wing of aspect ratio 10 undergoes a prescribed sinusoidal translational and rotational motion, described by

$$X(t) = \frac{1}{2}A_0 \cos(2\pi ft), \quad Y(t) = 0, \quad (9)$$

$$\alpha(t) = \alpha_0 + \beta \sin(2\pi ft + \Phi). \quad (10)$$

The angle,  $\alpha$ , is measured counterclockwise relative to the positive  $x$  axis. No mean flow is present in these simulations, which are meant to represent insect hovering aerodynamics. The maximum translational velocity of the wing centroid,  $U_{\max}$ , is  $\pi A_0 f$ . For comparison with the simulations and experiments of Wang et al. [28], the initial angle,  $\alpha_0$ , is  $\pi/2$ , and the rotational amplitude,  $\beta$ , is  $\pi/4$ , for all simulations. The translational amplitude,  $A_0$ , is  $2.8c$ , where  $c$  is the chord length of the wing, and thus the maximum translational velocity of the wing centroid,  $U_{\max}$ , is  $8.8c/T$ , where  $T$  is the flapping period. The frequency,  $f$ , is 0.25 Hz, and the Reynolds number, based on  $U_{\max}$  and  $c$ , is 75. As found in [28] and several prior investigations, the phase,  $\Phi$ , of rotation relative to translation—which specifies the timing of the ‘flip’ in the turnaround of the wing—is a critical parameter in determining the magnitude of lift force developed by the flapping wing in hovering kinematics. In the simulations presented in this work, two phases are used: in the first, the wing rotation leads the translation by  $\Phi = \pi/4$ ; in the second, with  $\Phi = 0$ , the flip is synchronous with the turnaround.

The time step size used is  $U_{\max}\Delta t/c = 7.33 \times 10^{-3}$ , the particle spacing is  $\Delta x/c = 0.01$ , and 300 surface panels are distributed as described in Section 3. Remeshing is carried out every 6 time steps, and the particle trimming threshold,  $\epsilon_{\text{trim}}$ , is  $3.5 \times 10^{-4}$ . With these choices of parameters,  $v\Delta t/\Delta x^2 = 0.95$  and  $\Delta x/\Delta s_{\max} = 0.95$ , well within the stability margins discussed in Section 3. The particle Reynolds number remains below 1.6 throughout the simulations. The particle spacing exceeds the minimum radius of curvature by a factor of two; decreasing the particle spacing to half the original value leads to no significant change in the results, as evident in the vertical force over a half-period depicted in Fig. 5 for the case  $\Phi = 0$ . Fig. 6 depicts the total circulation in the extended vorticity field (i.e. in the fluid and within the body) for  $\Phi = \pi/4$ , which should be identically zero by Kelvin’s circulation theorem. The procedure used in this work leads to very good enforcement of this constraint. The accuracy of the enforcement is determined by the error tolerance of the least-squares solution procedure for the vortex sheet strength.

Fig. 7 depicts the vorticity field produced during the third and fourth cycles when the flip occurs prior to turnaround,  $\Phi = \pi/4$ . The extent of the stroke is illustrated in the first panel by a dashed line. At the initiation of a new cycle, the wing is oriented with a large positive angle of attack with respect to its new direction of motion (to the left). A large vortex of positive circulation adjacent to the lower side of the wing is immediately absorbed into the boundary layer during the initial acceleration. A starting vortex is shed from the trailing edge, while a leading edge vortex of clockwise sense is formed. This leading edge vortex remains attached throughout the translation and is ‘recaptured’ by the wing during the subsequent rotation and deceleration. Successive vortices shed from the trailing edge pair to form vortex dipoles that propagate obliquely downward. The wake does not grow extensively below the stroke plane, as older vortices that have been weakened

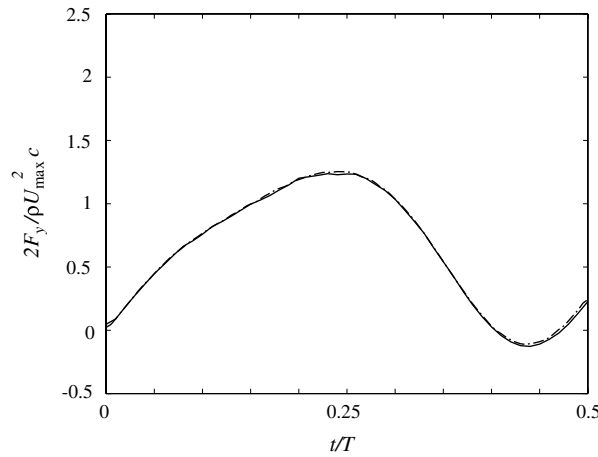


Fig. 5. Vertical force component for a phase of 0, using two different resolutions:  $\Delta x/c = 0.01$ , —, and  $\Delta x/c = 0.005$ , - -.

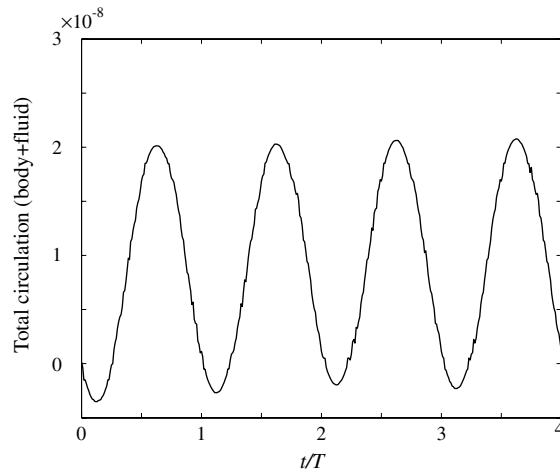


Fig. 6. Total circulation (in the fluid, plus that associated with body rotation) versus time, for phase  $\pi/4$ .

by viscous diffusion are entrained by newer ones. The large-scale velocity field induced by the flapping is revealed by evaluating the Biot–Savart integral in a region of dimensions  $[30c, 30c]$ . The result at  $t/T = 3.5$  is shown in Fig. 8, with the vorticity field included for reference. The vectors are given uniform length in this figure to emphasize the sense of the field. The dipolar nature of the farfield velocity is clearly apparent in this plot, exhibiting a downward jet whose mean momentum flux balances the mean upward force on the wing.

The lift and drag on the wing are defined, respectively, as the force components directed upward ( $F_y$ ) and opposite the direction of translation ( $-F_x U/|U|$ ). These components are depicted in Fig. 9 and compared with the three-dimensional experimental and two-dimensional computational results of Wang et al. [28]. The geometric differences are scaled out by normalizing the force components on each wing by the maximum steady forces on the wing in fixed configuration. The resulting mean lift is 0.639 and the mean drag is 0.589 from the VVPM simulations. The lift is in good agreement with the simulations of [28] over the first stroke, but the lift from both simulations generally disagrees with the experimentally-measured value during these early stages. In later strokes, the peak values of the lift from the VVPM match well with those from the experiments of [28], though the character of the lift between peaks is quite different; the peaks of the simulations of [28] are generally smaller. The drag is in reasonable agreement for all techniques. It should also be noted that the three-dimensional simulations of Gilmanov and Sotiropoulos [17], using their hybrid Cartesian/immersed-boundary method, agreed well with similar experiments conducted previously by Birch and Dickinson [18].

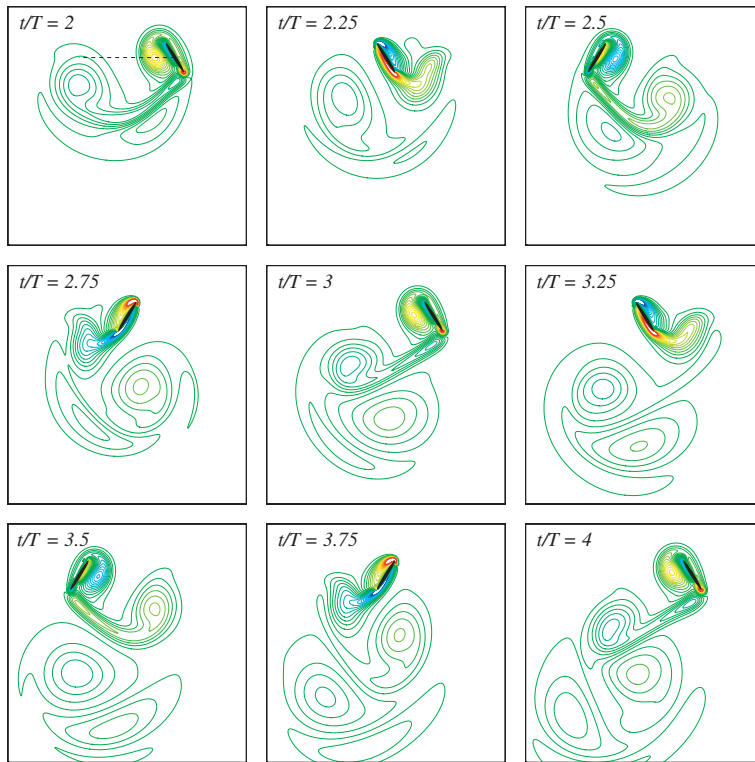


Fig. 7. Vorticity field at the labeled instants for phase  $\pi/4$ , with 40 contour levels distributed uniformly between  $-20$  and  $20$ .

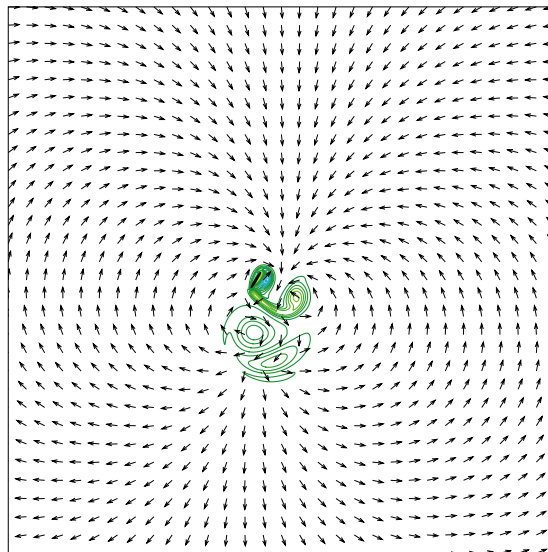


Fig. 8. Vorticity field (color contours) and velocity direction field at  $t/T = 3.5$  for phase  $\pi/4$ .

The sensitivity to kinematics can be observed by comparing the results from this case with those for a phase  $\Phi = 0$ . The vorticity dynamics for this latter case, depicted in Fig. 10, are remarkably similar to the previous case, exhibiting the same behavior of leading edge vortex recapture and trailing edge vortex shedding. However, the characters of the lift and drag, as shown in Fig. 11, differ significantly from those of the previous case.

20 and 20.

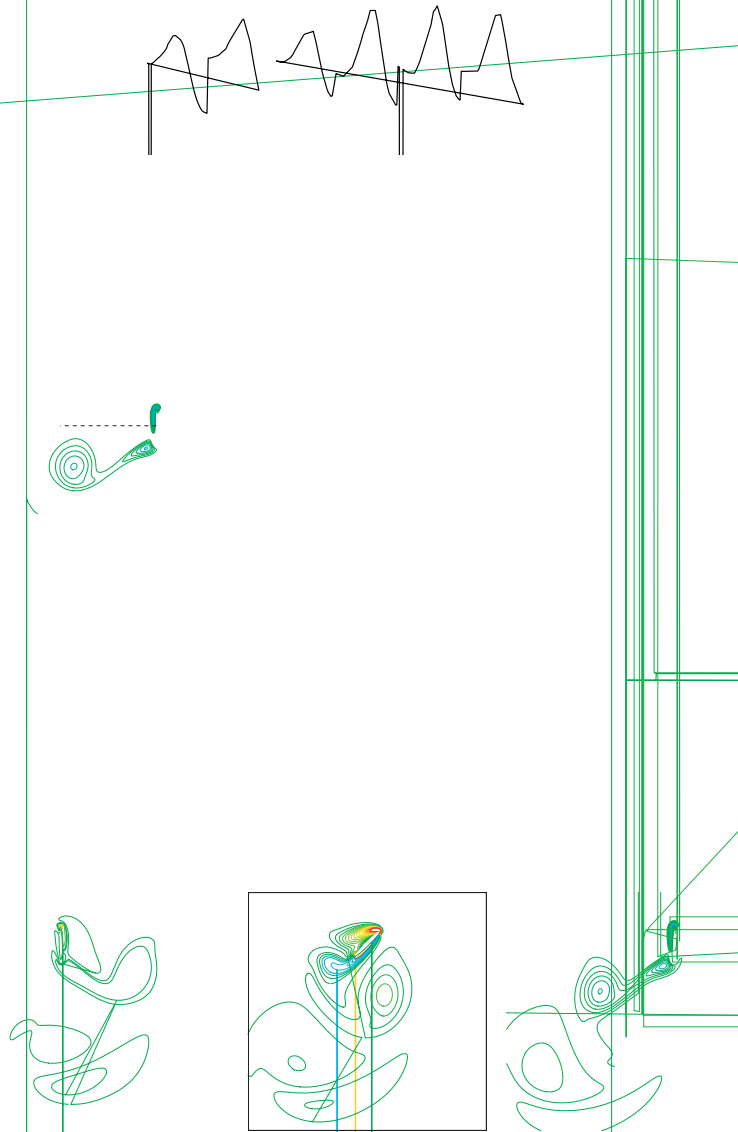


Fig. 10. Vorticity field at the labeled instants for phase 0, with 40 contour levels distributed

The agreement between the simulations is very good, and these results also match favorably with the experiments. The mean lift is 0.515, somewhat smaller for these kinematics than the previous case. The peak value of the drag is also smaller, but the mean drag is larger at 0.726, and the end of each half-cycle is characterized by a larger negative drag component.

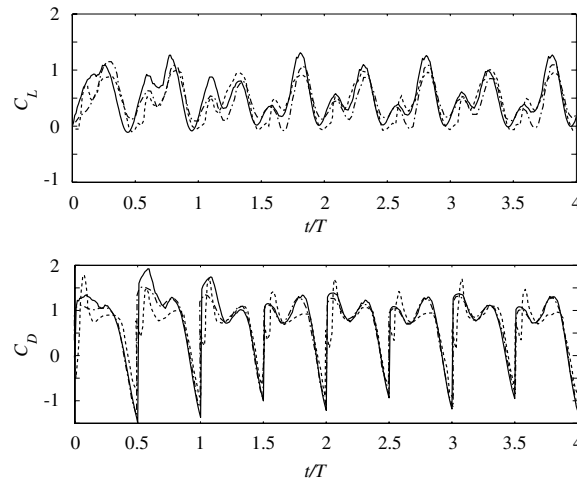


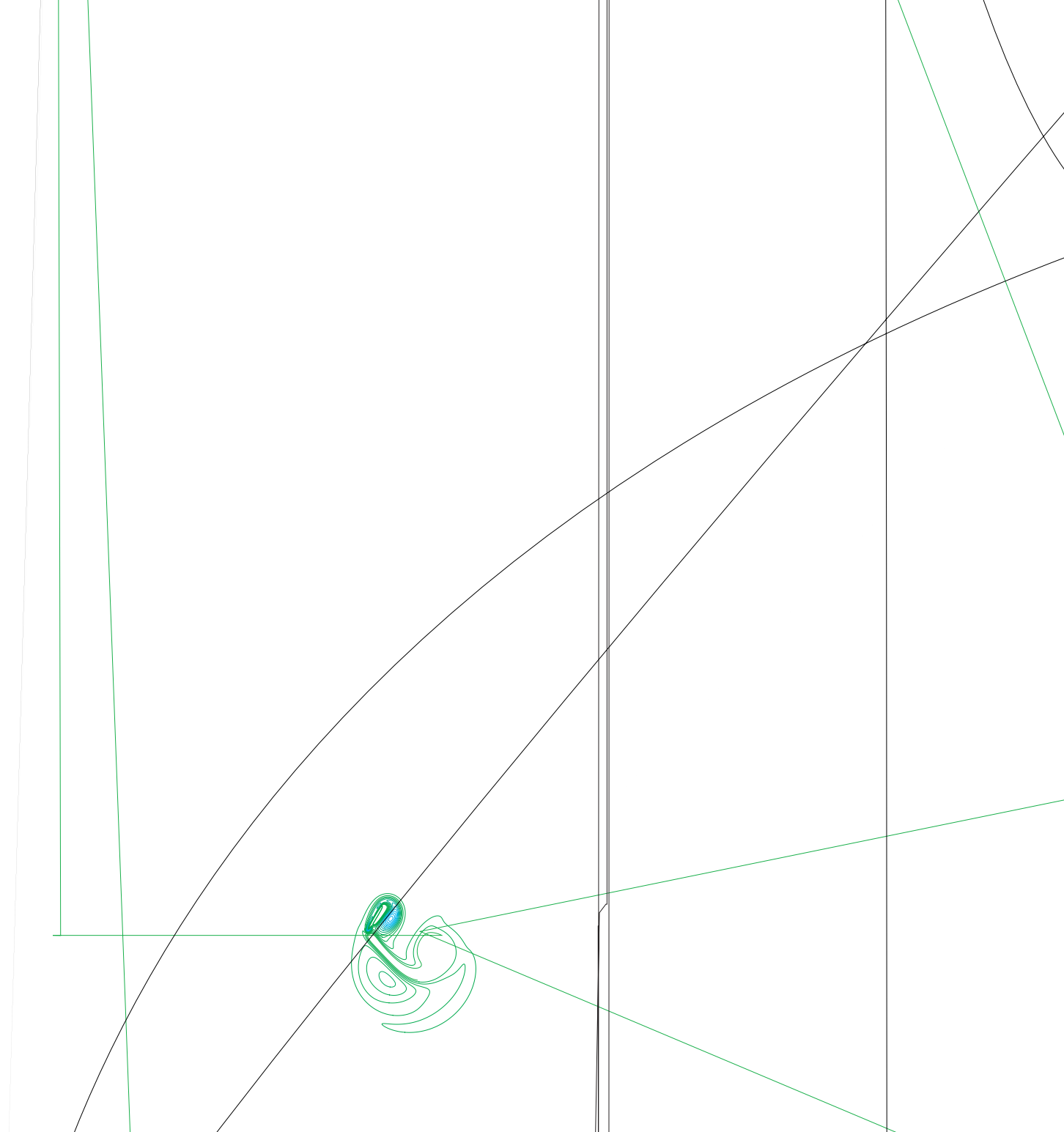
Fig. 11. Lift and drag coefficients, normalized by maximum quasi-steady values, for hovering mode with phase 0. VVPM simulation: —; WBD 2D simulation: - - -; WBD 3D experiment: ···.

The time-varying vorticity flux distribution elucidates the connection between vortex shedding and force generation. Fig. 12(a) and (c) depicts the force contributions from the pressure and shear stress for  $\Phi = \pi/4$  and  $\Phi = 0$ , respectively, over the same half-stroke; plots (b) and (d) show the corresponding vortex sheet strength distributions at the four instants labeled in (a) and (c). Note that the force has been normalized with the conventional  $\rho U_{\max}^2 c/2$  in these plots. In the distribution plots,  $\phi$  is the same parameterization used for paneling, with  $\phi = 0$  at the trailing edge, and proceeding in counterclockwise fashion around the wing. The shear stress contribution is much smaller than that of the pressure, so attention is focused on this latter component. The first maximum is labeled (1) and is plotted with a solid line in the distribution. This maximum coincides with the generation of a starting vortex at the trailing edge, which is evident in a peak in  $\gamma$  near  $\phi = 0$ . The maximum occurs later in the  $\Phi = 0$  case, and is here partly attributable to the formation of a leading edge vortex, manifested in the negative peak at  $\phi = \pi/2$  in (d). The second maximum (3) is more substantial in both cases, and is coincident with large negative fluxes at the leading edge. It occurs at nearly the same instant in both cases, soon after the maximum translational velocity has been reached. The final force minimum (4) occurs when the leading edge velocity is nearly zero and the flux into the leading edge vortex has weakened substantially.

The computational time of the VVPM depends primarily on the rate of growth of the number of particles, which is controlled by the trimming parameter,  $\epsilon_{\text{trim}}$ . The effect of this parameter is exhibited in the two panels in Fig. 13, which depict the instantaneous vorticity field (for  $\Phi = \pi/4$ ) and the boundary of particle coverage for  $\epsilon_{\text{trim}} = 3.5 \times 10^{-4}$  and  $3.5 \times 10^{-3}$ , respectively. In the former case, the particle boundary encloses a large region containing low-level values of unplotted vorticity; this low-level vorticity has been discarded with the larger trim threshold. Very little difference between the vorticity fields is discernible, except for slight variation in the shapes of wake vortices. Fig. 14 shows that the force coefficients also match very closely, except for small disagreement at  $t/T = 1$  and  $t/T = 3$ . The particle population growth in Fig. 14 demonstrates the clear importance of choosing  $\epsilon_{\text{trim}}$  judiciously: an order of magnitude increase in this threshold leads to half the number of particles, and therefore, half the computation time. These simulations have been performed on a workstation with dual AMD Opteron 246 processors and 2 Gb of memory; the CPU time per time step versus the number of particles, plotted in Fig. 15, confirms the  $O(N)$  scaling.

#### 4.2. Prescribed undulatory motion of a three-linkage fish

The final example of this work consists of a linked system of three identical elliptical bodies, each of length  $c$  and aspect ratio 10. The motion of the rigid links are constrained by virtual hinges that are a fixed distance,  $d = 0.2c$ , from the nearest centroid (see Fig. 16). The configuration of this system is completely described by



the angle  $\beta$  that the central body makes with the positive  $x$  axis, the coordinates of the centroid of this body,  $(X_0, Y_0)$ , and the hinge angles,  $\theta_1$  and  $\theta_2$ . The trajectory prescribed to this configuration, depicted in Fig. 17, is the solution of the *inviscid free swimming* problem, recently carried out by Kanso et al. [29]. In this previous analysis, the remaining system configuration was determined by solving the coupled dynamics of body and fluid in response to the hinge inputs,

$$\theta_1 = \Omega_m \cos(t - t_0), \tag{11}$$

$$\theta_2 = \Omega_m \cos(t - t_0 - \pi/2). \tag{12}$$



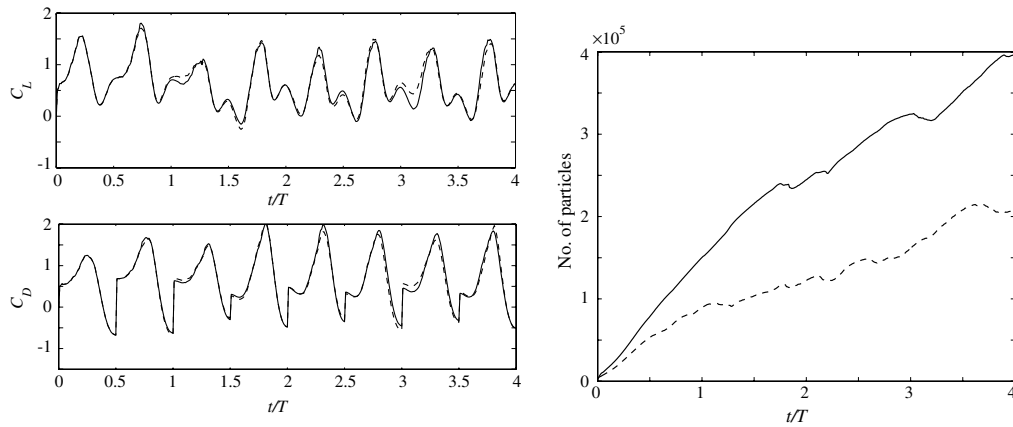


Fig. 14. Lift and drag coefficients (left) and evolution of number of particles (right), for  $\epsilon_{\text{trim}} = 3.5 \times 10^{-4}$  (—) and  $3.5 \times 10^{-3}$  (---), for phase  $\pi/4$  case.

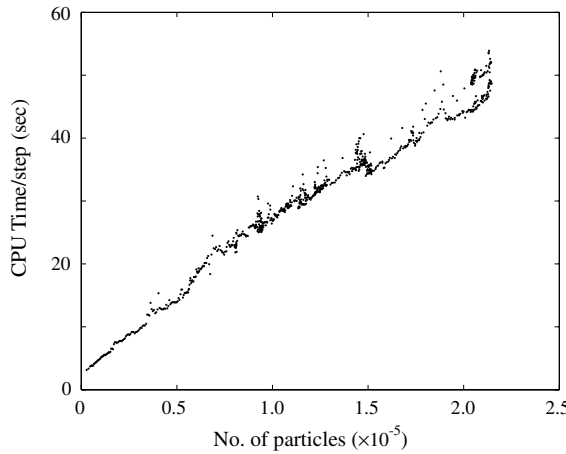


Fig. 15. CPU time per step versus number of particles for flapping wing,  $\Phi = \pi/4$ , for  $\epsilon_{\text{trim}} = 3.5 \times 10^{-3}$ .

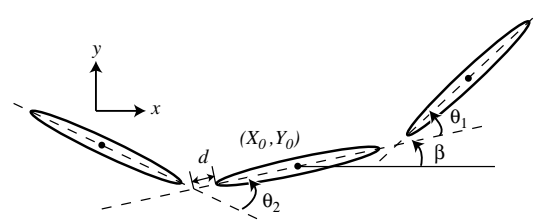


Fig. 16. Diagram of three-linkage fish.

These inputs represent a lowest-order form of undulatory kinematics employed by, for example, anguilliform fish. For  $\Omega_m = 1$  and  $t_0 = \pi$ , these inputs cause the fish to travel in an inviscid medium at a mean angle of approximately  $-20^\circ$  to the  $x$  axis, at a mean forward speed,  $\bar{U}_f$ , of approximately  $2.7c$  per period, or  $0.43\Omega_m c$ . The maximum speed of the leading edge of the fish during this motion is  $1.58\Omega_m c$ .

In the present viscous solution, the Reynolds number (based on the chord of a single body and the maximum angular velocity of each hinge,  $Re = \Omega_m c^2/\nu$ ) is chosen to be 200. The particle spacing is  $\Delta x/c = 0.01$ ,

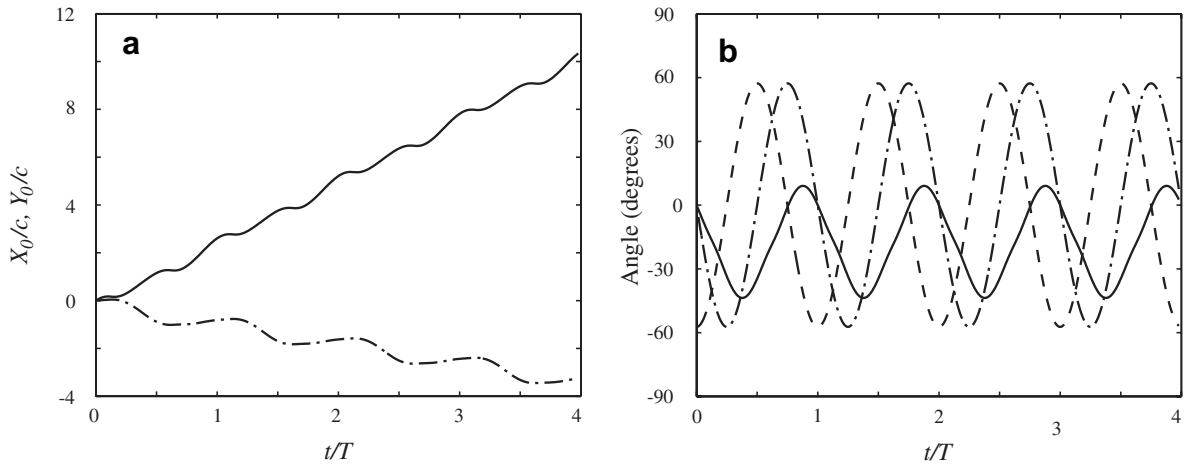


Fig. 17. (a) Prescribed coordinates of centroid of central body of three-linkage fish.  $X_0/c$ : —;  $Y_0/c$ : - - -. (b) Prescribed angles of fish.  $\beta$ : —;  $\theta_1$ : - -;  $\theta_2$ : - . - .

and the time step size is  $\Omega_m \Delta t = 0.01$ . Each wing is composed of 280 panels, with sizes ranging between  $0.0011c$  and  $0.011c$ . Thus,  $v\Delta t/\Delta x^2 = 0.5$  and  $N_p \Delta x/c = 2.8$ , ensuring a stable computation. The trim threshold,  $\epsilon_{\text{trim}}$ , is set to  $2 \times 10^{-3}$ . The growth of the number of particles is depicted in Fig. 18; after four periods of undulation, the number of particles is  $2.1 \times 10^5$ . During the course of the simulation, the particle Reynolds number never exceeds a value of 2, and simulation with finer resolution and smaller trim threshold does not lead to significant change in the results.

The vorticity field produced by this motion is depicted in the stacked frames of Fig. 19, with the overall trajectory of the fish depicted in the last frame. The largest magnitudes are generated at the leading and trailing edges of the bodies as they turn, and these edge vortices are shed into a relatively narrow boundary layer. The wake is composed of alternating sign vortices shed from the trailing edge of the tail. The resultant force exerted on the fish, shown in Fig. 20, is nearly periodic after a single cycle. The component in the direction perpendicular to motion (counterclockwise from the direction of travel) is characterized by a large positive peak followed by an equally large negative one, representing the reaction of the fluid to the lateral heaves of the fish. The parallel force component (positive in the direction of motion) is also characterized by positive

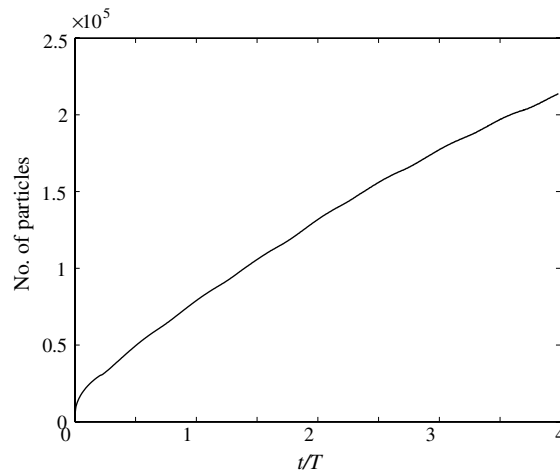
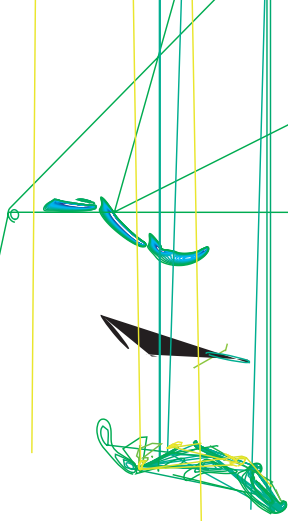
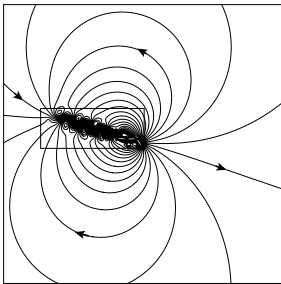
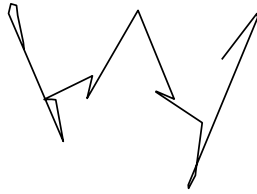


Fig. 18. Growth of number of particles for three-linkage fish.



and negative peaks; the average component is  $-0.083\Omega_m^2 c^3$ , indicating a net drag. The mean drag coefficient, defined with  $\rho \bar{U}_i^2 c/2$ , is 0.90.

The streamfunction field shown at  $t/T = 4$  in Fig. 21 is consistent with a net drag on the body. The dipole pattern at large distances is reminiscent of that associated with a translating cylinder, rather than a self-locomotive system which would exhibit a rearward jet. The streamfunction field of the wake exhibits entrainment of fluid, which is necessary to compensate for the momentum defect. In the free swimming solution, the fish accelerates until the mean parallel force component is zero. In the present constrained motion, the fish is effectively attached to external rods that are moved in a predefined way; when the mean resultant force exerted on these rods is zero, then the system is in equilibrium and the prescribed motion approaches the free swimming trajectory. In the present case, the prescribed forward motion is faster than the equilibrium speed at this Reynolds number.



## 5. Conclusions

In this work, the implementation of a vortex particle method for simulating two-dimensional rigid bodies in a viscous fluid has been described, and its application to example problems has been presented. An important aspect of the present implementation is the simplified particle treatment near the body. Particles are initially arranged in a Cartesian mesh rather than conforming to the body surface, and the interpolation during remeshing is carried out in a ‘body-ignorant’ fashion with symmetric kernels. Circulation that leaks into the body during this interpolation is re-introduced to the flow by the subsequent vortex sheet diffusion, so that Kelvin’s circulation theorem remains enforced. The vorticity flux corrects any spurious slip introduced during this leak correction. Numerical studies have shown that the residual slip converges to zero in the limit of vanishing particle spacing. These studies have also showed that the boundary treatment imposes a lower bound on the viscous parameter,  $\nu\Delta t/\Delta x^2$ , in addition to its usual upper bound from time-marching schemes.

The applications presented in this work have demonstrated the utility of this tool for simulating rigid body motion in fluids, and the results of two-dimensional flapping wing simulations have agreed well with previous numerical and experimental studies. The present method provides direct access to some quantities, such as the vorticity flux at the body surface and the velocity field at large distances, that can provide new physical insight in fluid–body interaction problems. The method has also recently been extended to problems with dynamic coupling between the body and fluid, such as in self-propagation of the three-linkage swimmer considered here, and this will be the subject of a future paper. Further development of the method, including improvements in efficiency and extension to three-dimensional deforming bodies, is currently being pursued for simulating more realistic models of biolocomotion.

## Appendix A. Body surface discretization

In this appendix, the mathematical details of the surface panel discretization in the VVPM are described. Each body surface is discretized by a set of linear panels, and a total of  $N_p$  panels is used. Each panel has  $N_g$  Gauss–Legendre quadrature points, with scaled positions  $\xi_j \in [0, 1]$  and associated weights  $w_j$ . In the global coordinate system, the position of the  $j$ th quadrature point on panel  $i$  is given by

$$\mathbf{x}_s(s_{ij}) = \mathbf{x}_{s,i} + \frac{1}{2} \Delta s_i \boldsymbol{\tau}_i (2\xi_j - 1). \quad (\text{A.1})$$

In this expression,  $\Delta s_i$  is the panel length and  $\mathbf{x}_{s,i}$  is the position of the panel centroid; the panel tangent vector,  $\boldsymbol{\tau}_i$ , is in the direction of increasing  $s$ , counterclockwise about the body.

### A.1. Particle position equations

The positions of the vortex particles are updated according to the Biot–Savart integral, with the surface integral from body vorticity discretized by the panels and associated quadrature points:

$$\frac{d\mathbf{x}_p}{dt} = \mathbf{U}_\infty + \sum_q V_q \omega_q(t) \nabla^\perp G_e(\mathbf{x}_p, \mathbf{x}_q) + 2 \sum_{k=1}^{N_p} \sum_{l=1}^{N_g} \Omega_{b(k)} \boldsymbol{\tau}_k w_l \Delta s_k G(\mathbf{x}_p, \mathbf{x}_s(s_{kl})). \quad (\text{A.2})$$

Here,  $\mathbf{x}_q$  is the position,  $V_q$  the area and  $\omega_q$  the vorticity strength of particle  $q$ . The smoothed Green’s function of the negative Laplacian is denoted by  $G_e$ . Note that  $\Omega_{b(k)}$  is equal to the angular velocity of the body to which panel  $k$  is fixed.

### A.2. Surface vortex sheet equation

Here we describe the procedure for solving the integral equation for the surface vortex sheet strength. The discretized and averaged equation can be represented mathematically as

$$\begin{aligned} \frac{1}{2} \gamma_i + \sum_{j=1}^{N_g} w_j \sum_{k=1}^{N_p} \gamma_k \Delta s_k \sum_{l=1}^{N_g} \frac{\partial G}{\partial n}(\mathbf{x}_s(s_{ij}), \mathbf{x}_s(s_{kl})) w_l \\ = -\boldsymbol{\tau}_i \cdot (\mathbf{u}_b(\mathbf{x}_{s,i}) - \mathbf{U}_\infty) - \frac{1}{L_i} \sum_{m \in \overline{\mathcal{P}}_i} \sum_{j=1}^{N_g} w_j \Delta s_m \sum_p \frac{\partial G}{\partial n}(\mathbf{x}_s(s_{ij}), \mathbf{x}_p) V_p \omega_p \\ + 2 \sum_{j=1}^{N_g} w_j \sum_{k=1}^{N_p} \Omega_{b(k)} \mathbf{n}_i \cdot \mathbf{n}_k \Delta s_k \sum_{l=1}^{N_g} G(\mathbf{x}_s(s_{ij}), \mathbf{x}_s(s_{kl})) w_l. \end{aligned} \quad (\text{A.3})$$

This expression has been evaluated at panel  $i$ , and  $\gamma_i$  is the sheet strength corresponding to this panel. The triple summation on the left-hand side represents the evaluation of the vortex sheet integral. In this term, the kernel represents the influence of the  $l$ th quadrature point of the  $k$ th panel on the  $j$ th quadrature point on the  $i$ th panel; the net influence on the panel is averaged over the quadrature points. On the right-hand side, the summation involving  $\omega_p$  represents the influence of the (non-regularized) vortex particles on panel  $i$ . This term involves an average over a set of panels  $\overline{\mathcal{P}}_i$ , centered at panel  $i$ , and with total length

$$L_i = \sum_{m \in \overline{\mathcal{P}}_i} \Delta s_m. \quad (\text{A.4})$$

The set  $\overline{\mathcal{P}}_i$  generally includes five panels: the panel  $i$  itself, and two panels on either side of  $i$ . The last term on the right-hand side of Eq. (A.3) represents the effect of body vorticity, which in this case is rigid-body rotation, and its influence on panel  $i$  is an average over the influences on the  $N_g$  quadrature points of panel  $i$ .

For elliptical bodies with the panel discretization (4), some numerical advantage can be gained by reformulating the equations in terms of the panel circulation,  $\tilde{\Gamma}_i = \gamma_i \Delta s_i$ . The  $N_p$  relations (A.3) can be written as a matrix system for the  $N_p$  panel circulations,  $\tilde{\Gamma}_i$  (after multiplying each term by a factor of 2) as

$$\sum_{k=1}^{N_p} \tilde{A}_{ik} \tilde{\Gamma}_k = \tilde{b}_i, \quad i = 1, \dots, N_p, \tag{A.5}$$

where

$$\tilde{A}_{ik} = \delta_{ik} + 2 \sum_{j=1}^{N_g} \sum_{l=1}^{N_g} \frac{\partial G}{\partial n}(\mathbf{x}_s(s_{ij}), \mathbf{x}_s(s_{kl})) w_j w_l \Delta s_i \tag{A.6}$$

and

$$\begin{aligned} \tilde{b}_i = & -2\boldsymbol{\tau}_i \Delta s_i \cdot (\mathbf{u}_b(\mathbf{x}_{s,i}) - \mathbf{U}_\infty) - \frac{2\Delta s_i}{L_i} \sum_{m \in \mathcal{P}_i} \sum_{j=1}^{N_g} w_j \Delta s_m \sum_p \frac{\partial G}{\partial n}(\mathbf{x}_s(s_{ij}), \mathbf{x}_p) V_p \omega_p \\ & + 4 \sum_{j=1}^{N_g} \sum_{k=1}^{N_p} \Omega_{b(k)} \mathbf{n}_i \cdot \mathbf{n}_k \sum_{l=1}^{N_g} G(\mathbf{x}_s(s_{ij}), \mathbf{x}_s(s_{kl})) w_j w_l \Delta s_i \Delta s_k. \end{aligned} \tag{A.7}$$

### A.3. Solution of linear system

The system of equations (A.5) is solved simultaneously with the constraint imposed on each of the  $N_b$  bodies by Kelvin’s circulation theorem. The discretized version of Eq. (1) is

$$\sum_{k=1}^{N_p} A_k^K \tilde{\Gamma}_k = b_j^K, \tag{A.8}$$

where

$$A_k^K = \begin{cases} 1, & k \in \mathcal{P}_b(j), \\ 0, & \text{otherwise.} \end{cases} \tag{A.9}$$

$\mathcal{P}_b(j)$  is the set of panels on the surface of body  $j$ , and  $b_j^K$  is the corresponding constraint,

$$b_j^K = -2A_j(\Omega_j(t + \Delta t) - \Omega_j(t)) + \Gamma_{\text{lost},j}. \tag{A.10}$$

Therefore, the complete system consists of  $N_p + N_b$  equations for  $N_p$  unknowns, which can be written as

$$\sum_{k=1}^{N_p} A_{ik} \tilde{\Gamma}_k = b_i, \quad i = 1, \dots, N_p + N_b, \tag{A.11}$$

where the first  $N_p$  rows of  $A_{ik}$  and  $b_i$  are equal to the corresponding rows of  $\tilde{A}_{ik}$  and  $\tilde{b}_i$ , respectively, and the last  $N_b$  rows are

$$A_{i+N_p,k} = \lambda A_{ik}^K, \quad b_{i+N_p} = \lambda b_i^K \tag{A.12}$$

for  $i = 1, \dots, N_b$ . The parameter  $\lambda$  can be chosen to improve the conditioning of the overall system; however, satisfactory results are obtained with unity. The overconstrained system (A.11) is solved in a least-squares sense by iteratively solving the square system

$$A^T A \tilde{\Gamma} = A^T b, \tag{A.13}$$

using the GMRES algorithm [42] with a solution tolerance of  $10^{-10}$ .

### A.4. Evaluation by fast multipole expansion

The influences of the vortex sheet, the body vorticity, and the fluid vorticity can each be accounted for in a computationally efficient manner with the fast multipole method. This method accelerates the computation of the potential field (and its derivatives) created by a distribution of singular sources of Laplace’s equation. In



two-dimensional flow, one can write the velocity field at  $\mathbf{x}$  resulting from a distribution of point vortices (with strengths  $\Gamma_p$  and positions  $\mathbf{x}_p$ ) and point sources (with strengths  $Q_q$  and positions  $\mathbf{y}_q$ ) as

$$\mathbf{u}(\mathbf{x}) = \sum_p \nabla^\perp G(\mathbf{x} - \mathbf{x}_p) \Gamma_p - \sum_q \nabla G(\mathbf{x} - \mathbf{y}_q) Q_q. \quad (\text{A.14})$$

The particle position equation (A.2) and the surface vortex sheet equation (A.3) are each given a fast multipole treatment. To prepare the terms in Eq. (A.3) for this treatment, the expression is slightly rewritten in the form,

$$\begin{aligned} & \tilde{\Gamma}_i - 2\boldsymbol{\tau}_i \cdot \sum_{j=1}^{N_g} w_j \Delta s_i \sum_{k=1}^{N_p} \sum_{l=1}^{N_g} \nabla^\perp G(\mathbf{x}_s(s_{ij}), \mathbf{x}_s(s_{kl})) (\tilde{\Gamma}_k w_l) \\ &= -2\boldsymbol{\tau}_i \cdot \left\{ \mathbf{u}_b(\mathbf{x}_{s,i}) - \mathbf{U}_\infty - \frac{\Delta s_i}{L_i} \sum_{m \in \mathcal{P}_i} \sum_{j=1}^{N_g} w_j \Delta s_m \sum_p \nabla^\perp G(\mathbf{x}_s(s_{ij}), \mathbf{x}_p) \Gamma_p \right. \\ & \quad \left. - \sum_{j=1}^{N_g} w_j \Delta s_i \sum_{k=1}^{N_p} \sum_{l=1}^{N_g} G(\mathbf{x}_s(s_{ij}), \mathbf{x}_s(s_{kl})) (2\Omega_{b(k)} \boldsymbol{\tau}_k \Delta s_k w_l) \right\}. \end{aligned} \quad (\text{A.15})$$

The fluid vorticity term has its usual form, as a collection of point vortices. In both the vortex sheet and the body vorticity terms, an effective potential strength has been identified and written in parentheses; in the vortex sheet term, this strength is just the Gauss-weighted circulation of panel  $k$ , whereas in the body vorticity term, the velocity components are essentially two potential fields created by a source distribution with vector strengths. Thus, these surface strengths and their associated quadrature positions can be sent to the multipole routine, in which the potentials (and derivatives of potentials) are evaluated at the target set of surface quadrature points. The subsequent averaging is carried out on the values returned by this routine.

In particular, the two matrix-vector products required for iteratively solving Eq. (A.13) can each be evaluated using this approach. The left-hand side of this equation is calculated out in two steps: first, the first  $N_p$  rows of the intermediate vector  $\boldsymbol{\sigma} = A\tilde{\Gamma}$  are computed by panel-to-panel multipole expansion (the final  $N_b$  rows are simple summations). Then  $A^T\boldsymbol{\sigma}$  is evaluated by another panel-to-panel multipole expansion. Note that,

$$A^T\boldsymbol{\sigma} = [\tilde{A}^T(A^K)^T]\boldsymbol{\sigma} = \tilde{A}^T\boldsymbol{\sigma}^{(1)} + (A^K)^T\boldsymbol{\sigma}^{(2)}, \quad (\text{A.16})$$

where  $\boldsymbol{\sigma}^{(1)}$  represents the first  $N_p$  rows of  $\boldsymbol{\sigma}$ , and  $\boldsymbol{\sigma}^{(2)}$  the final  $N_b$  rows. Similarly,  $A^T\tilde{b} = \tilde{A}^T\tilde{b} + (A^K)^T b^K$ . Then, the matrix-vector product  $\tilde{A}^T\boldsymbol{\sigma}^{(1)}$  is given by

$$(\tilde{A}^T\boldsymbol{\sigma}^{(1)})_i = \sigma_i^{(1)} + 2 \sum_{j=1}^{N_g} w_j \sum_{k=1}^{N_p} \sum_{l=1}^{N_g} \nabla^\perp G[\mathbf{x}_s(s_{ij}), \mathbf{x}_s(s_{kl})] \cdot \boldsymbol{\tau}_k \sigma_k^{(1)} \Delta s_k w_l, \quad (\text{A.17})$$

where we have used the fact that  $\nabla^\perp G(\mathbf{x}, \mathbf{x}') = -\nabla^\perp G(\mathbf{x}', \mathbf{x})$ . Now, it is easy to show that

$$\boldsymbol{\tau}_x \nabla^\perp G - \boldsymbol{\tau}_y \nabla G = \begin{pmatrix} \nabla^\perp G \cdot \boldsymbol{\tau} \\ -\nabla G \cdot \boldsymbol{\tau} \end{pmatrix}. \quad (\text{A.18})$$

Thus, the product  $\nabla^\perp G \cdot \boldsymbol{\tau}$  is equal to the first component of the vector  $\boldsymbol{\tau}_x \nabla^\perp G - \boldsymbol{\tau}_y \nabla G$ . This last expression represents the velocity field associated with a potential vortex of strength  $\tau_x$  and a coincident source of strength  $\tau_y$ , so Eq. (A.17) can be written as

$$(\tilde{A}^T\boldsymbol{\sigma}^{(1)})_i = \sigma_i^{(1)} + 2 \sum_{j=1}^{N_g} w_j \sum_{k=1}^{N_p} \sum_{l=1}^{N_g} \{ \tau_{k,x} \nabla^\perp G[\mathbf{x}_s(s_{ij}), \mathbf{x}_s(s_{kl})] - \tau_{k,y} \nabla G[\mathbf{x}_s(s_{ij}), \mathbf{x}_s(s_{kl})] \}_x \sigma_k^{(1)} \Delta s_i w_l. \quad (\text{A.19})$$

This observation allows the use of the multipole routine to evaluate the product  $\tilde{A}^T\boldsymbol{\sigma}^{(1)}$ . A similar technique is used to evaluate  $\tilde{A}^T\tilde{b}$ . The remaining terms,  $(A^K)^T\boldsymbol{\sigma}^{(2)}$  and  $(A^K)^T b^K$ , are straightforward to evaluate.

## References

- [1] K. Gustafson, R. Leben, Computation of dragonfly aerodynamics, *Comput. Phys. Commun.* 65 (1991) 121–132.
- [2] Z.J. Wang, Vortex shedding and frequency selection in flapping flight, *J. Fluid Mech.* 410 (2000) 323–341.
- [3] M. Sun, J. Tang, Unsteady aerodynamic force generation by a model fruit fly wing in flapping motion, *J. Exp. Biol.* 205 (2002) 55–70.
- [4] M.H. Dickinson, F.-O. Lehmann, S.P. Sane, Wing rotation and the aerodynamic basis of insect flight, *Science* 284 (1999) 1954–1960.
- [5] H. Liu, K. Kawachi, A numerical study of insect flight, *J. Comput. Phys.* 146 (1998) 125–156.
- [6] C. van den Berg, C.P. Ellington, The vortex wake of a ‘hovering’ model hawkmoth, *Phil. Trans. R. Soc. Lond. B* 352 (1997) 317–328.
- [7] R. Ramamurti, W.C. Sandberg, A three-dimensional computational study of the aerodynamic mechanisms of insect flight, *J. Exp. Biol.* 205 (2002) 1507–1518.
- [8] T. Ye, R. Mittal, H.S. Udaykumar, W. Shyy, An accurate Cartesian grid method for viscous incompressible flows with complex immersed boundaries, *J. Comput. Phys.* 156 (1999) 209–240.
- [9] H.S. Udaykumar, R. Mittal, P. Rampunggoon, A. Khanna, A sharp interface Cartesian grid method for simulating flows with complex moving boundaries, *J. Comput. Phys.* 174 (2001) 345–380.
- [10] R. Mittal, Y. Utturkar, H.S. Udaykumar, Computational modeling and analysis of biomimetic flight mechanisms, *AIAA Paper* 2002-0865, 2002.
- [11] C.S. Peskin, Numerical analysis of blood flow in the heart, *J. Comput. Phys.* 25 (1977) 220–252.
- [12] M.-C. Lai, C.S. Peskin, An immersed boundary method with formal second-order accuracy and reduced numerical viscosity, *J. Comput. Phys.* 160 (2000) 705–719.
- [13] L.J. Fauci, C.S. Peskin, A computational model of aquatic animal locomotion, *J. Comput. Phys.* 77 (1988) 85–108.
- [14] L.A. Miller, C.S. Peskin, A computational fluid dynamics of ‘clap and fling’ in the smallest insects, *J. Exp. Biol.* 208 (2005) 195–212.
- [15] J. Mohd-Yusof, Combined immersed-boundaries/B-splines methods for simulations of flows in complex geometries, Technical Report, CTR Annual Research Briefs, Stanford University, 1997.
- [16] E.A. Fadlun, R. Verzicco, P. Orlandi, J. Mohd-Yusof, Combined immersed-boundary finite-difference methods for three-dimensional complex flow simulations, *J. Comput. Phys.* 161 (2000) 35–60.
- [17] A. Gilmanov, F. Sotiropoulos, A hybrid Cartesian/immersed boundary method for simulating flows with 3D, geometrically complex, moving boundaries, *J. Comput. Phys.* 207 (2005) 457–492.
- [18] J.M. Birch, M.H. Dickinson, The influence of wing-wake interactions on the production of aerodynamic forces in flapping flight, *J. Exp. Biol.* 206 (2003) 2257–2272.
- [19] D. Russell, Z.J. Wang, A cartesian grid method for modeling multiple moving objects in 2D incompressible viscous flow, *J. Comput. Phys.* 191 (2003) 177–205.
- [20] M.J. Lighthill, Introduction: boundary layer theory, in: L. Rosenhead (Ed.), *Laminar Boundary Layers*, Clarendon Press, Oxford, 1961.
- [21] T. Sarpkaya, Computational methods with vortices—The 1988 Freeman Scholar Lecture, *J. Fluids Eng.* 111 (1989) 5–52.
- [22] P. Koumoutsakos, Multiscale flow simulations using particles, *Ann. Rev. Fluid Mech.* 37 (2005) 457–487.
- [23] P. Koumoutsakos, A. Leonard, F. Pépin, Boundary conditions for viscous vortex methods, *J. Comput. Phys.* 113 (1994) 52–61.
- [24] P. Degond, S. Mas-Gallic, The weighted particle method for convection-diffusion equations, Part 1: The case of an isotropic viscosity, *Math. Comp.* 53 (188) (1989) 485–507.
- [25] P. Ploumhans, G.S. Winckelmans, Vortex methods for high-resolution simulations of viscous flow past bluff bodies of general geometry, *J. Comput. Phys.* 165 (2000) 354–406.
- [26] G.-H. Cottet, P. Koumoutsakos, M.L.O. Salihi, Vortex methods with spatially varying cores, *J. Comput. Phys.* 162 (2000) 164–185.
- [27] G.-H. Cottet, P. Poncet, Advances in direct numerical simulations of 3D wall-bounded flows by vortex-in-cell methods, *J. Comput. Phys.* 193 (2003) 136–158.
- [28] Z.J. Wang, J.M. Birch, M.H. Dickinson, Unsteady forces and flows in low Reynolds number hovering flight: two dimensional computations vs robotic wing experiments, *J. Exp. Biol.* 207 (2004) 449–460.
- [29] E. Kanso, J.E. Marsden, C.W. Rowley, J. Melli-Huber, Locomotion of articulated bodies in a perfect fluid, *J. Nonlinear Sci.* 15 (4) (2005) 255–289.
- [30] G.-H. Cottet, P. Koumoutsakos, *Vortex Methods: Theory and Practice*, Cambridge University Press, Cambridge, 2000.
- [31] J. Carrier, L. Greengard, V. Rokhlin, A fast adaptive multipole algorithm for particle simulations, *SIAM J. Sci. Stat. Comput.* 9 (4) (1988) 669–686.
- [32] J.D. Eldredge, A. Leonard, T. Colonius, A general deterministic treatment of derivatives in particle methods, *J. Comput. Phys.* 180 (2002) 686–709.
- [33] W. Prager, Die druckverteilung an köperen in ebener potentialströmung, *Physik. Zeitschr.* 29 (1928) 865–869.
- [34] P. Koumoutsakos, A. Leonard, Improved boundary integral method for inviscid boundary-condition applications, *AIAA J.* 31 (2) (1993) 401–404.
- [35] A. Leonard, D. Shiels, J.K. Salmon, G.S. Winckelmans, P. Ploumhans, Recent advances in high resolution vortex methods for incompressible flows, *AIAA Paper* 97-2108, 1997.
- [36] J.J. Monaghan, Particle methods for hydrodynamics, *Comp. Phys. Rep.* 3 (1985) 71–124.

- [37] P. Koumoutsakos, D. Shiels, Simulations of the viscous flow normal to an impulsively started and uniformly accelerated flat plate, *J. Fluid Mech.* 328 (1996) 177–227.
- [38] P. Koumoutsakos, Direct numerical simulations of unsteady separated flows using vortex methods, Ph.D. Thesis, California Institute of Technology, 1993.
- [39] R.J. Leveque, Z. Li, The immersed interface method for elliptic equations with discontinuous coefficients and singular sources, *SIAM J. Numer. Anal.* 31 (4) (1994) 1019–1044.
- [42] Y. Saad, M. Schultz, GMRES: a generalized minimal residual algorithm for solving nonsymmetric linear systems, *SIAM J. Sci. Stat. Comput.* 7 (3) (1986) 856–869.